Icarus ••• (••••) •••–•••

Contents lists available at ScienceDirect

Icarus

www.elsevier.com/locate/icarus

A dynamical model of the sporadic meteoroid complex

Paul Wiegert [a,*], Jeremie Vaubaillon [b], Margaret Campbell-Brown [a]

[a] Dept. of Physics and Astronomy, The University of Western Ontario, London, Canada
[b] Spitzer Space Center, Jet Propulsion Laboratory, California Institute of Technology, Pasadena, CA 91125, USA

ARTICLE INFO

Article history:
Received 31 October 2008
Revised 19 December 2008
Accepted 19 December 2008
Available online xxxx

Keywords:
Meteors
Comets
Asteroids
Interplanetary dust
Earth

ABSTRACT

Sporadic meteoroids are the most abundant yet least understood component of the Earth's meteoroid complex. This paper aims to build a physics-based model of this complex calibrated with five years of radar observations. The model of the sporadic meteoroid complex presented here includes the effects of the Sun and all eight planets, radiation forces and collisions. The model uses the observed meteor patrol radar strengths of the sporadic meteors to solve for the dust production rates of the populations of comets modeled, as well as the mass index. The model can explain some of the differences between the meteor velocity distributions seen by transverse versus radial scatter radars. The different ionization limits of the two techniques result in their looking at different populations with different velocity distributions. Radial scatter radars see primarily meteors from 55P/Tempel–Tuttle (or an orbitally similar lost comet), while transverse scatter radars are dominated by larger meteoroids from the Jupiter-family comets. In fact, our results suggest that the sporadic complex is better understood as originating from a small number of comets which transfer material to near-Earth space quite efficiently, rather than as a product of the cometary population as a whole. The model also sheds light on variations in the mass index reported by different radars, revealing it to be a result of their sampling different portions of the meteoroid population. In addition, we find that a mass index of $s = 2.34$ as observed at Earth requires a shallower index ($s = 2.2$) at the time of meteoroid production because of size-dependent processes in the evolution of meteoroids. The model also reveals the origin of the 55° radius ring seen centered on the Earth's apex (a result of high-inclination meteoroids undergoing Kozai oscillation) and the central condensations seen in the apex sources, as well as providing insight into the strength asymmetry of the helion and anti-helion sources.

1. Introduction

The meteoroid population is traditionally broken down into two components. The first is the "stream meteoroids," which follow orbits around the Sun that are strongly correlated with each other. These orbits are also often closely correlated with that of the parent body which released the particles, since the ejection process produces changes to the velocity which are typically small compared to the orbital velocity. Over time, the stream of meteoroids produced by the parent may move to a markedly different orbit or split into several separate streams as differential perturbations due to the planets, radiation effects, etc. modify their orbits in various ways (Vaubaillon et al., 2006). Eventually, perturbations accumulate and disperse the meteoroid stream, the original close orbital relationship between individual meteoroids becoming difficult to determine.

At this point, the particles have become part of the second component of the meteoroid population, the "sporadic meteoroids," which form a more diffuse but far from isotropic background flux of particles. The division of streams and sporadics, though somewhat artificial, remains useful nonetheless. Since the time-integrated flux of visual meteors at Earth is dominated by about a factor of 10 by sporadics (Jones and Brown, 1993), models of the near-Earth environment are incomplete without serious consideration of the sporadic meteoroids.

Once released from their parent body, be it comet or asteroid, the smallest meteoritic particles ($\lesssim$0.1 μm) will be ejected by radiation forces (the so-called β meteoroids). Larger ones continue to orbit the Sun. Unlike the planets whose substantial mass keeps them rather firmly on their orbits, meteoroids are subjected to a variety of influences which change their orbits over time. These effects include the gravity of the planets, Poynting–Robertson and solar wind drag, and collisions.

Here we present the results of a physics-based model of the sporadic complex which numerically integrates the orbits of meteoroids from their ejection from a parent body through to their eventual destruction or loss from the Solar System. Our work par-

* Corresponding author. Fax: +1 519 661 2033.
E-mail address: pwiegert@uwo.ca (P. Wiegert).

0019-1035/$ – see front matter
doi:10.1016/j.icarus.2008.12.030

allels in some ways that of the ESA meteoroid model (Landgraf et al., 2001; Dikarev et al., 2002, 2004). In fact, the ESA meteoroid model incorporates more observational constraints than our own, including many obtained by spacecraft, while we rely only on Earth-bound radar measurements. Nevertheless, our simple model can answer a number of outstanding questions relating to the sporadic meteoroid complex.

The construction of our model presents many challenges. There are hundreds of known comets, each producing dust at variable (and largely unknown) rates, so dust production must be estimated. Meteoroids in the inner Solar System may persist for millions of years, so the current sporadic complex likely contains particles that originated from parents that are long dead or otherwise lost. The inhabitants of the sporadic complex are truly astronomical in number, a heterogeneous collection of cometary and asteroidal particles, too numerous to simulate in their entirety. Given the number of free parameters and their degeneracy, we have chosen to construct our model on the pillars of simplicity and physicality. In other words, we will keep the number of free parameters of the model to a minimum and link them clearly to physical processes. Thus our emphasis will be on the construction of a physically meaningful model and then examining how it does or does not reproduce observations rather than fine-tuning the model at the expense of understanding its inner workings.

The primary free parameters in our model are the relative dust contributions of the various parent objects of the sporadic complex, and we will fit these parameters to match meteoroid fluxes at Earth, a process we call "calibration" (Section 4.1). We allow five parameters, one for each of the five meteoroid parent populations we examine: the Jupiter-family comets (JFCs), the prograde and retrograde Halley-family comets (HFCs, which we examine separately but ultimately assign equal dust production coefficients), the asteroid belt and the near-Earth asteroids. Thus all the myriad details of the variability between parent objects of a particular type are encapsulated in a single free parameter. We also allow a single free parameter for the slope of the size distribution, also be fitted to observations. This brings the total number of tunable parameters in the model to six.

It is worth emphasizing the centrality of this procedure. Instead of assuming a dust production rate or size distribution, we instead use radar observations of the sporadic meteors to fit these parameters, replacing rather poorly known quantities with very well known ones.

In the construction of our model, our biggest assumptions are that

1. The five parent populations each produce dust at fixed rates which remain constant with time.
2. The current orbits of the parent objects simulated are representative of those of all parent orbits over the lifetime of a typical sporadic meteor (0.1–10 Myr).
3. No meteoroids are produced by sources other than the known comets and asteroids.
4. The properties of the dust are independent of the parent, and the size distribution produced is a fixed power-law.

Insofar as these assumptions hold, our model can be expected to reproduce the observed sporadic complex. We will see that in fact the broad strokes of the observed sporadic complex are reproduced by such a model, including the radiant, velocity and orbital element distributions. Section 2 outlines our simulation code and methods, Section 3 details the meteoroid source populations used here, Section 4 discusses how we calibrate the model, Section 5 presents our discussion of the results, and our conclusions are presented in Section 6.

2. Methods

Our simulated Solar System includes the Sun and all eight major planets with masses, positions and velocities derived from the JPL DE405 ephemeris (Standish, E.M., 1998. Planetary and lunar ephemerides DE405/LE405. Technical report, NASA Jet Propulsion Laboratory). The simulations of the meteoroids were performed with one of two simulation codes, with a few portions run on both codes and compared to ensure they were producing similar results. The first of these codes was a symplectic integrator based on the Wisdom–Holman algorithm (Wisdom and Holman, 1991) with close approaches handled by the hybrid method (Chambers, 1999), coded and used by PW (time step = 7 days unless otherwise noted). The second was a Radau integrator (Everhart, 1985) coded and used by JV (variable time step set initially to 1 day). Both these codes are mature and well-tested. The simulations include the effects of Poynting–Robertson drag, solar radiation pressure and collisions.

2.1. Meteoroid modeling

2.1.1. Cometary meteoroids

Cometary meteoroid ejection is modeled by the Crifo and Rodionov (1997) cometary ejection model. Comets are all assumed to have a Bond albedo of 0.04, a density of 1000 $\mathrm{kg\,m^{-3}}$, a radius of 1 km and an active fraction of 0.2. Ejection was usually begun at 3 AU, though in a few cases of comets with larger perihelion distances q (*i.e.* 74P and 31P) the ejection process was started further out at 4 AU.

The meteoroids simulated ranged in radius from 10 μm to 10 cm, distributed uniformly in the log of their radius (*i.e.* a histogram of number N binned over $\log(r)$ is flat). This size distribution was designed to produce sufficient number statistics at all sizes, and was re-weighted according to the observed size distribution of meteoroids at the end (see Section 2.2.2).

Each parent (of which there are 38, parent selection is described in Section 3.1) produces 4000 meteoroid particles released during a single perihelion passage. As a simulation progresses, these meteoroids represent older and older members of the overall population. Snapshots of the simulated meteoroids are recorded at intervals, and the ensemble of the meteoroid orbits recorded during the simulation provide us with the evolution of the meteoroid complex over time. Thus an effective number of 8×10^5 meteoroids of varying ages are produced per parent, or 38 parents × 4000 particles × 200 snapshots = 30.4 million meteoroids in total.

2.1.2. Asteroidal meteoroids

Asteroidal dust production is modeled in two ways. The dust production of near-Earth asteroids is handled the same as cometary dust (*i.e.* by the Crifo and Rodionov, 1997 model). However, dust from the main belt is generated differently. Instead of being ejected from a parent body, a suite of 4000 particles of sizes 10 μm to 10 cm is initially randomly distributed in the asteroid belt. These meteoroids have initial elements of $2 < a < 3.3$ AU, $0 < e < 0.3$ and $0^\circ < i < 30^\circ$, to which was added a random velocity kick of 3 km/s. These orbital elements were chosen to represent the debris of collisions between asteroids in the densest portion of the main belt, debris which may be a dominant source of meteoroids in near-Earth space (Dermott et al., 2002a). The velocity of 3 km/s was chosen as being typical of collision velocities in the main belt (Vedder, 1998). It is worth noting that collisions in the main belt are not violent enough to put much material directly onto Earth-crossing orbits. However, meteoroids from the main belt may eventually reach the Earth (if not destroyed in subsequent collisions) through the effects of P–R drag and orbital resonances, particularly with Jupiter and Saturn.

Please cite this article in press as: Wiegert, P., et al. A dynamical model of the sporadic meteoroid complex. Icarus (2009), doi:10.1016/j.icarus.2008.12.030

2.1.3. Simulation details

The length of time the simulations need to be run is a function of the particles' lifetime against collisions (with each other and the Sun and planets) and ejection. The collisional lifetimes of particles is $\lesssim 10^5$ yr for particles near the Earth in the ecliptic plane (Grun et al., 1985). These collisional lifetimes are increased for particles with higher inclinations or larger orbits, and so the simulations described here are all run from 10^5 to 2.5×10^6 yr depending on the orbit of the parent. The simulations are subsequently checked to verify that there is at most only a small fraction (*e.g.* $\lesssim$10%) of meteoroids that have not been removed or destroyed by the end of the simulation. A complete simulation of all particles until their demise is impractical as a few particles will inevitably have very long lifetimes while contributing negligibly to the overall flux at the Earth.

Meteoroids are removed from the simulations if they fall into the Sun, move beyond 1000 AU or collide with a planet. They are also removed if their age exceeds the collisional lifetime determined for meteoroids in our Solar System (see Section 2.2.8). Ideally one would like to incorporate collisions in a more realistic way, perhaps by looking for collisions between meteoroids directly during the simulations. This is unfortunately impractical with today's computing capabilities, as the number of meteoroids N in the simulation would have to match those of the real Solar System in order to correctly match collision rates, and looking for collisions requires computational efforts that goes like N^2. This puts the problem into the near-impossible category.

However, we can say something about the effects of collisions, and how best to treat them. Grun et al. (1985) discuss some of the effects of collisions and allow us to make some approximate statements about their likely outcomes. They find that for masses $>10^{-3}$ g ($r = 340$ μm at $\rho = 2000$ kg m^{-3}) about 10 times more mass is destroyed by impacts than generated; that for masses from 10^{-4} to 10^{-6} g (160–34 μm) about equal numbers of particles are removed as are generated; and that for masses below 10^{-6} g (below 34 μm) collisions generate more particles than they destroy. This allows us to conclude that over most of our range of sizes, collisions result in a net reduction or little effect on the overall mass distribution of the particles, with collisional fragments going mainly into smaller sizes. So the effect of collisions on the particle size distribution in our region of interest is primarily one of removal, though we recognize that we may be missing a significant injection of particles at the smallest sizes modeled here.

2.2. Weighting

Our simulations follow an equal number of meteoroids from each parent, so we have to deal with determining the relative contributions of the different parent objects to the total. We call this process "weighting." There are five factors and three cutoffs which we apply to produce the proper weighting of a simulated meteoroid, listed below.

2.2.1. Sublimation and perihelion distance

Dust production by individual parent objects is taken to be proportional to the amount of ice sublimated. Ice sublimation is known to start at approximately $r_0 = 3$ AU from the Sun (Delsemme, 1982; Spinrad, 1987) and the time average rate of sublimation W_s can be shown (Jones, J., 2002. A model of the sporadic meteoroid complex. Technical report, The University of Western Ontario and NASA (MSFC)) to be

$$W_s = \frac{\theta_c(1-e)^2}{q^2\sqrt{1-e^2}}, \tag{1}$$

where

$$\theta_c = \arccos\left(\frac{q(1+e)-r_0}{r_0 e}\right) \tag{2}$$

is the true anomaly at which the distance to the Sun is r_0. Note that some comets show dust production at larger distances, likely owing to the presence of more volatile ices such as CO and CO_2. We use $r_0 = 3$ AU in our simulations (with the exception of 31P and 74P, which use $r_0 = 4$ AU owing to their larger perihelia), with dust production assumed to be uniform throughout the perihelion passage.

2.2.2. Size distribution of meteoroids

Our simulations are run with a differential particle size distribution which is constant in logarithmic space. This allows adequate sampling of all sizes while giving some additional coverage of the smaller particles which are more abundant.

However, our simulated distribution does not match reality and thus must be weighted appropriately to match the observed distribution. Conveniently, for a distribution that is flat in log space like ours, the weighting W_r required to adjust the particle distribution to a differential distribution with $dN/dr \propto r^\alpha$ is just $W_r = r^{\alpha+1}$.

The observed meteoroid size distribution can be approximated by a power-law $dN(m) \propto m^{-s}\,dm$, where $s \approx 2.34$ (Whipple, 1967; Grun et al., 1985). Since $m \propto r^3$, this implies that $dN(r) \propto r^{-3s+2}\,dr \approx r^{-5.0}\,dr$. So the weighting needed to match the observations is $W_r \propto r^{-3s+3} \approx r^{-4.0}$.

The $r^{-5.0}$ power-law illustrates why a realistic size distribution was not used in the simulations. Since our size range spans about 4 orders of magnitude (10 μm to 10 cm), we would have to simulate approximately $(10^4)^5 = 10^{20}$ meteoroids at the smallest size for each one at the largest size, making for impractically many particles at small sizes and very poor statistics at the larger sizes.

To be more precise, the weighting factor W_r chooses the mass index of the ejected dust distribution, not that observed at Earth. In fact, a meteoroid size distribution of $dN/dr \propto r^\alpha$ at the source need not produce the same power-law slope (or even necessarily a power-law) at the Earth. Size-dependent evolution of the meteoroids, including the effects of P–R drag and size-dependent collision lifetimes may modify the size distribution observed at Earth. However we will see that the power-law size distribution is largely retained among meteoroids which intersect the Earth, though with a modified slope (Section 5.1).

Here we choose W_r so as to reproduce the $s = 2.34$ mass distribution at the Earth over the size range of 100 μm to 1 cm, in order to best match the size range at which the determination is made. Thus, we actually weight the particles according to $W_r = r^{-3.6}$ (instead of $r^{-4.0}$), this value empirically determined to return the particle size distribution seen at Earth to the correct slope. The resulting model size distribution at Earth is discussed further in Section 5.1.

2.2.3. Collision probability with Earth

The model computes the orbits of meteoroids and determines which of those orbits pass close to the Earth in order to determine the population of Earth-intersecting meteoroids. We take those which pass within 0.1 AU of the Earth's orbit as our sample, a compromise between accuracy and the need for a sufficiently large number of particles to conduct a relevant statistical analysis (Öpik, 1976). Each orbit must be weighted to account for the fact that intersecting orbits do not necessarily imply that the meteoroid will be near the Earth at any given time.

The encounter probability (the probability that any given meteoroid is within 0.1 AU of the Earth at a given instant) required here is similar to the classic result of Öpik (1976) but differs slightly as our sample already consists specifically of intersecting orbits, rather than randomly oriented orbits. The derivation is similar however, and the final result for the weighting factor is just

$$W_c \propto \frac{2D}{|\dot{r}|a^{1.5}}, \tag{3}$$

where a is the particle's semimajor axis and $\dot{r}$ is the radial component of its velocity. D is not a characteristic of each individual orbit, but is the radius of the torus inside which the orbit is deemed Earth-intersecting (0.1 AU in this model). The application of this weighting transforms our distribution of orbits to a number density of meteoroids in near-Earth space. A further factor of V_∞, the relative velocity of the meteoroid with respect to the Earth, would transform the density into a flux, which is most convenient for comparison with meteor observations.

There are two possible singularities in Eq. (3), if a or $\dot{r}$ are zero. The first case doesn't happen in practice so we can ignore it, but the possibility of $\dot{r} \approx 0$ near the Earth is non-negligible, occurring if the particle crosses the Earth's orbit just at perihelion or aphelion. This singularity can easily be dealt with, however. The $\dot{r}$ arises from a term $D/|\dot{r}|$ representing the time the particle spends near the Earth's orbit. This number blows up if the crossing takes places near the particle's perihelion or aphelion, and so is replaced by a simple numerical computation of how much time the particle spends within D of the Earth's orbit. Though an important consideration overall, it only occurs for a small percentage of the orbits in question and so we do not do a full numerical treatment for all particles, as it is time-consuming and produces only a small improvement in other cases.

2.2.4. Gravitational focusing

The model considers the set of all particles whose orbits pass within 0.1 AU of the Earth's orbit to be the population which the Earth itself intercepts, whether or not the Earth is present at the time. As a result, an additional correction term is added to allow for the gravitational focusing which the real Earth exerts on meteoroids. This term accounts for the fact that slower-moving meteoroids will be more easily drawn into impact with Earth, adding a slight additional weight to slow meteoroids versus fast ones. The weighting factor W_g is given by Öpik (1976)

$$W_g = 1 + (V_{\rm esc}/V_\infty)^2, \tag{4}$$

where V_∞ is the velocity of the meteoroid when far from the Earth and $V_{\rm esc}$ is the Earth's escape velocity (11.2 km/s).

2.2.5. Number of comets per bin

Many of the JFCs simulated act as proxies for other comets with similar a, e and i (see Section 3.1.1). As a result, their contribution to the meteoroid flux is multiplied by the number of comets N they represent, adding a fifth and final additional weighting factor $W_p = N$.

2.2.6. Earth intersection cutoff

In addition to the five weighting factors, there are three sample cutoffs to be considered. The first cutoff involves the extraction of those orbits which intersect the Earth. Even given the large number of simulated meteoroids, too few meteoroids impact the Earth (passing, say, within a hundred km of the surface) for us to reliably determine meteor fluxes in near-Earth space this way. Rather we select out those meteoroids with orbits that bring them within 0.1 AU of the Earth's orbit as those which constitute the meteoroid flux at Earth. Note we do not simply select based on nodal distance being near the Earth, but rather compute the actual closest approach distance between a meteoroid and the Earth's orbit. If this distance is less than 0.1 AU, the meteoroid is included in our sample. This method avoids the possibility of missing particles which pass near the Earth but which do not have nodes near the Earth, a possibility which occurs for very low inclination orbits.

2.2.7. Removal of shower meteors

The second of the cutoffs involves the removal of shower meteors. Showers are removed by disregarding all particles which arrive at the Earth in less than a particular amount of time τ_s, which varies from parent to parent. This number was determined empirically from a visual inspection of the radiant size and its duration in time. As the transition from shower to sporadic is often one of gradual diffusion, without a sharp boundary, we adopt a criterion where the meteoroids are no longer deemed to be part of a shower if their arrival at the Earth is spread over more than a month in time. This definition is necessarily fuzzy for a number of reasons, which can be traced to the difficulty in unambiguously defining a "meteor shower." Nevertheless, this provides a good first cut at removing very young collimated streams from the model.

The value of τ_s used here varies from zero to 500 years for sources which do not produce noticeable showers at Earth (such as many JFCs and the asteroid belt), up to 250000 years in a few cases (*e.g.* Comet Thatcher, parent of the Lyrids). This variation is due to the varying stability of the orbit of the parent body and of the frequency of close approaches to the planets. Note that since we sample the meteoroids at 500 year intervals in most cases, we are insensitive to values of τ_s which are less than this. However, since showers which are shorter-lived than 500 yr do not appear in our results, they are effectively removed anyway and do not constitute a problem here. Table 1 lists the values of τ_s determined. Note that the results of the model appear to be insensitive to the choice of τ_s though we have not investigated this in great detail.

2.2.8. Collisional lifetimes

The third and final cutoff is the removal of meteoroids deemed to have exceeded their collisional lifetime. Collisions are handled by ascribing to each meteoroid in the simulation a collisional lifetime based on its orbital elements. Since the orbits of meteoroids change over time and the collisional lifetime is sensitive to the details of the orbit, we must account for this fact. We do this by summing up the collisional probability over time. In practice, we assume that a meteoroid has reached the end of its collisional lifetime when its summed collisional probability p_c equals 1. The probability of collision occurring during a time interval dt a meteoroid spends on an orbit with lifetime $T(a, e, i, \Omega, \omega)$ is just dt/T and so we take the meteoroid to have reached the end of its collisional lifetime when

$$\int_0^t p_c = \int_0^t \frac{dt}{T(a, e, i, \Omega, \omega)} = 1. \tag{5}$$

In practice, the integral is changed to a summation where we take the sum over the individual snapshots (Section 2.1.1), over each of which the orbit is assumed to be effectively constant.

The lifetime T used here is based on those of Steel and Elford (1986) and Grun et al. (1985). Steel and Elford (1986) is used as the basis for the model because they account for the meteoroid's orbit (a, e, i), an important factor. The Grun et al. (1985) model is used to supplement this because of its careful accounting for the effects of different particle sizes, since Steel and Elford compute lifetimes only for a particle radius r of 1 mm. Here we take the Steel and Elford lifetime and then multiply it by $T_G(r)/T_G(1\ \text{mm})$, where T_G is the Grun et al. lifetime. As a result, our collisional lifetime has the orbital dependence of Steel and Elford (1986) (that is T is taken to be a function only of a, e and i), and the size dependence of Grun et al. (1985). Meteoroids that are older than their collisional lifetimes as described above are removed from the model. Note we extrapolate Grun et al.'s collisional lifetimes to up to sizes of 1000 g from their upper limit of 100 g.

Table 1
The parent objects used in the model. W_p is the number of parent objects this body represents (see Section 2.2.5). τ_s is the age (in units of 10^3 yr) below which meteoroids are deemed to be stream meteors rather than sporadics. A $*$ represents a special case (see text for more details).

Name	W_p	a (AU)	q (AU)	e	i (deg)	Ω (deg)	ω (deg)	τ_s
2P/Encke	4	2.216	0.338	0.847	11.769	334.587	186.499	0.5
3D/Biela	3	3.525	0.860	0.755	12.550	248.004	223.191	0.5
4P/Faye	14	3.837	1.657	0.568	9.049	199.338	204.975	0.5
6P/d'Arrest	14	3.493	1.352	0.612	19.497	138.945	178.113	0.5
7P/Pons–Winnecke	8	3.438	1.258	0.634	22.284	93.449	172.292	0.5
9P/Tempel 1	3	3.121	1.506	0.517	10.530	68.937	178.839	0.5
10P/Tempel 2	4	3.070	1.426	0.535	12.017	117.848	195.558	0.5
14P/Wolf	6	4.069	2.412	0.407	27.522	204.120	162.363	0.5
16P/Brooks	18	3.611	1.834	0.491	5.548	176.913	198.108	0.5
17P/Holmes	10	3.682	2.165	0.412	19.187	328.010	23.347	0.5
31P/S–W 2	9	4.235	3.408	0.195	4.549	114.194	18.403	0.5
32P/Comas–Sola	7	4.255	1.833	0.569	12.927	60.794	45.825	0.5
42P/Neujmin 3	2	4.855	2.014	0.585	3.985	150.385	147.160	0.5
53P/Van Biesbroeck	3	5.391	2.415	0.551	6.610	149.004	134.096	0.5
56P/Slaughter–Burnham	2	5.109	2.535	0.503	8.155	346.271	44.096	0.5
59P/Kearns–Kwee	2	4.468	2.339	0.476	9.352	313.035	127.446	0.5
63P/Wild 1	2	5.597	1.960	0.649	19.934	358.525	167.991	0.5
64P/Swift–Gehrels	3	4.383	1.338	0.694	8.437	306.140	92.413	0.5
65P/Gunn	6	3.589	2.445	0.318	10.384	68.416	196.375	0.5
74P/Smirnova–Chernykh	3	4.163	3.545	0.148	6.652	77.156	86.654	0.5
79P/duToit–Hartley	4	3.030	1.229	0.594	2.894	307.970	253.072	0.5
91P/Russell	3	3.888	2.601	0.330	14.092	247.897	354.699	0.5
140P/Bowell–Skiff	2	6.396	1.971	0.691	3.835	343.459	173.082	0.5
142P/Ge–Wang	2	4.995	2.496	0.500	12.173	177.139	177.385	1
1P/Halley	1	17.942	0.587	0.967	162.242	58.860	111.865	4
55P/Tempel–Tuttle	1	10.336	0.976	0.905	162.486	235.258	172.498	2
109P/Swift–Tuttle	1	26.316	0.958	0.963	113.426	139.444	153.001	20
8P/Tuttle	1	5.671	0.997	0.824	54.692	270.548	206.703	4
12P/Pons–Brooks	1	17.132	0.773	0.954	74.177	255.891	199.027	20
27P/Crommelin	1	9.090	0.732	0.919	29.100	250.501	195.841	0.5
35P/Herschel–Rigollet	1	28.840	0.748	0.974	64.207	355.980	29.298	20
122P/deVico	1	17.680	0.658	0.962	85.389	79.617	12.975	20
126P/IRAS	1	5.611	1.702	0.696	45.961	357.700	356.887	4
2003 EH_1	1	3.126	1.193	0.618	70.773	282.957	171.336	2
53430	1	2.098	1.250	0.404	60.421	241.968	156.860	10
66008	1	1.426	0.909	0.362	61.006	168.957	13.901	10
2003 QQ_{47}	1	1.085	0.882	0.187	62.100	1.011	105.009	7.5
Main asteroid belt	$*$	2–3.5	1.4–3.5	0–0.3	0–30	0–360	0–360	0

2.3. Final weighting

As a result of the above considerations, each meteoroid orbit is subject to a weighting term W given by

$$W = k_i W_s W_r W_c W_g W_p, \tag{6}$$

where the sum of all the weighting terms must add up to the observed flux of meteors. The term k_i is the dust production coefficient of the parent population in question. The k_i are the free parameters we must solve for to complete our weighting of the meteoroids, a step we refer to as "calibration," described in Section 4.1. Before discussing calibration, we first pass to a description of the parent populations simulated.

3. Source population

There are a wide variety of bodies throughout the Solar System which generate meteoroids. The sources of most interest here will be broken down into five categories. Two of these, the short-period comets and the long-period retrograde comets are already associated with the strong production of sporadic meteors, namely the helion/anti-helion and north/south apex source pairs respectively. Since we are using the meteor fluxes to determine the dust production rates of our parent populations, these sources can be modeled relatively straightforwardly as will be described in Sections 3.1.1 and 3.1.2.

Observationally, there is one other pair of strong sporadic sources which has not yet been unequivocally associated with a parent, namely the north and south toroidal sources. In Section 3.1.3 a combination of the prograde HFCs and the NEA population will be shown to provide an adequate but probably not unique parent population for this pair of sporadic sources.

Finally, the contribution of the asteroid belt to the sporadic meteoroid complex at Earth is largely unknown. Both radar and visual techniques are insensitive to meteors arriving at low-velocity, as asteroidal meteoroids typically do. The calculation of the asteroidal contribution to the model is described in Section 3.1.5. A discussion of the relative contributions of comets and asteroids to the low-velocity flux at Earth is in Section 5.7.

3.1. Selected sources

We divide our comets into two categories, one of which we call short-period or Jupiter-family comets (JFCs), the other long-period or Halley-family comets (HFCs). The division is made simply on the basis of orbital period, at the traditional 20 year boundary. The orbital data are taken from Marsden and Williams (2005).

3.1.1. Jupiter-family comets

There are 152 Jupiter-family comets known as of this writing with the "periodic" or "P/" designation, and are the sample of JFCs with the best determined orbits. Simulating meteoroid production by all 152 of the JFCs would be prohibitive in terms of time required (each comet modeled here requiring approximately 2 CPU-days), so we select a representative sample of JFCs to represent the whole. We gridded the phase space of the Jupiter family into 5 bins of semimajor axis a and eccentricity e, and 3 bins of inclination i, for 75 bins. The bins cover, in semimajor axis, 2.215 to 7.00 AU; in eccentricity, 0.0 to 0.85; and in inclination, 0 to 32°. The boundaries span the range of orbital elements for the Jupiter-family comets, with a few exceptions described below.

Only 40 of the 75 bins actually have a comet in them, and only 24 bins have more than one. We choose these 24 bins as our sample, and simulate one comet from this bin to represent the bin as a whole. We do not simulate bins with only one comet in them (with a few exceptions) for the following reason. Bins with two or more comets in them contain 134/152 = 88% of the JFCs. Thus we can effectively model about 90% of the total meteoroid production by doing full computations on only 24/152 or 16% of the comets. This gain in efficiency makes the problem much more tractable. The comets chosen are listed in Table 1.

In each bin, the comet with the lowest numerical periodic comet designation was usually chosen as the representative member. For example, in one bin are Comets 10P, 25D, 26P and 46P. In this bin, Comet 10P/Tempel was chosen. Since there is little information on dust production rates from most comets, we assumed here that the ones found first are brightest, most active, and contribute most to the dust environment. In some cases, we choose others, usually associated with meteor showers, since they are known to produce a lot of dust. In one case, a lost comet (3D/Biela) was chosen over the other two comets in its bin (24P/Schaumasse and 103P/Hartley) because it was lost only fairly recently, is likely to have produced a lot of meteoroids when it broke up, and is associated with a meteor shower (the Andromedids).

3.1.2. Retrograde long-period comets

The north and south apex sources are associated with the retrograde long-period comets due to orbital determinations from radar studies (Jones and Brown, 1993, and references therein). The dominant contributors are the bright periodic comets of this

type, and we can adequately model the apex sources using only Comets 1P/Halley, 55P/Tempel–Tuttle and 109P/Swift–Tuttle, each associated with one or more strong meteor showers, namely the η Aquarids and Orionids, the Leonids and the Perseids respectively.

3.1.3. Prograde long-period comets

The orbital distribution of the toroidals has a high inclination (around 70°). There are very few known possible parents with such parameters. As discussed in Section 3, the prograde long-period comets together with the NEAs provide the (empirical) best match to the toroidal sporadic meteor source of any of the bodies modeled here. Comet 8P/Tuttle, 12P/Pons–Brooks, 27P/Crommelin, 35P/Herschel–Rigollet, 122P/deVico and 126P/IRAS constitute the population of prograde HFCs with $i > 45°$, so if the toroidal source has a cometary parent, this is the sample that will include it. Comet C/1861 G1 Thatcher (parent of the April Lyrids meteor shower, $i = 79°$), Comet C/1917 F1 Mellish (associated with the December Monocerotids), 96P/Machholz and the Meyer group of Sun-grazing comets ($i \sim 72°$) were also examined, many requiring simulations with smaller time steps because of their low perihelion distances. However these were ultimately excluded (*i.e.* given zero weight and we do not list them in Table 1) because they produced strong sporadic sources that have not actually been observed.

3.1.4. Near-Earth asteroids

In addition to the comets examined in Section 3.1.3, a number of other potential toroidal parents were investigated, namely the near-Earth asteroids with suitably high inclinations. These included 2102 Tantalus, 3200 Phaethon, 5496, 10563 Izhdubar, 53430, 66008, 85818, 1998 UQ_1, 1999 TX_2, 2000 DK_{79}, 2001 AU_{43}, 2002 SS_{41}, 2003 EH_1, 2003 QQ_{47}, 2003 TS_9, 2006 BZ_7. Orbital data were obtained from the NeoDys website (http://newton.dm.unipi.it/cgi-bin/neodys/neoibo). Of these, few produced radiants consistent with the toroidal sources. Ultimately we included 2003 EH_1, 53430, 66008 and 2003 QQ_{47} as producing (together with the prograde HFCs) the best match with the toroidals (see Section 4.1 for more details) while the weights of the other NEAs are set to zero. None of the four included NEAs have been linked with meteor streams with the exception of 2003 EH_1, associated with the Quadrantid shower (Jenniskens, 2004; Williams et al., 2004; Wiegert and Brown, 2005).

3.1.5. Asteroid belt

The contribution of asteroids to the meteor flux at Earth is difficult to determine. Their low velocities relative to our planet mean that they are harder to detect by optical and radar means, so their flux is harder to measure. Nonetheless, they certainly arrive at Earth in some numbers, particularly at meter sizes and above as evidenced by the meteorite collections of the world. Asteroidal meteoroids are modeled as discussed in Section 2.1.2.

4. Calibration and verification

The radar meteor determination of the sporadic fluxes from the Canadian Meteor Orbit Radar (CMOR; Jones et al., 2005) will serve as our primary benchmark here, as it constitutes the largest and best-understood sample of sporadic meteors measured to date.

We will use the radar data set for two purposes. One is to scale the simulations to the correct flux rates for meteoroids in the size range CMOR observes best ("calibration"). This process allows us to remove to first-order the uncertainty in the dust production rates of our parent objects by simply matching them to observed meteor rates.

The second use we will have for the CMOR data is for comparison purposes and model validation. Here we will use the additional information provided by the orbital element distribution determined by CMOR, which is largely independent of the simple fluxes used for calibration.

4.1. Calibration

For our calibration, we weight the model meteoroid fluxes for the three sporadic meteor sources (anti-helion/helion, north/south apex and north/south toroidal) to match radar measurements. Here we used the CMOR observations of the helion and anti-helion sources combined, but since the south apex and south toroidal sources are more difficult or impossible for CMOR to observe due to geometry, the north apex and north toroidal fluxes are the ones used here.

In order to match the observing characteristics of the radar, the model sample is taken to a single limiting ionization, where the ionization I of any particular model meteor is given by

$$I = \frac{m}{10^{-7}\ \mathrm{kg}}\left(\frac{(V_\infty^2 + V_{\mathrm{esc}}^2)^{1/2}}{30\ \mathrm{km/s}}\right)^{3.5}. \quad (7)$$

The detection threshold of CMOR is an ionization of approximately one in these units (Campbell-Brown, 2008). We compare our model sample with a set of CMOR observations that have been corrected for collecting area and initial trail radius (the two largest bias corrections needed). Note that the radar observations used are not corrected to an effective limiting mass, in order to eliminate any assumptions about the mass distribution.

The model calibration involves selecting a dust production coefficient k_i for each of the five populations so as to match the strengths of the three observed sources. These are the five primary free parameters of the model. One of these, for the asteroid belt, will be chosen by other means as asteroidal meteors are not easily measured by radar (discussed below). Thus we are left with four unknowns and three constraints.

Our first considerations are the helion and anti-helion sporadic sources. These have long been known to have orbits closely resembling JFCs. These sources are the strongest observed by transverse scatter radar. We see negligible contributions from the HFCs and other parents to these sources in our model, so we can unambiguously determine the JFC component of our model. Here we set the dust production coefficient of a typical JFC to be $k_{\mathrm{JFC}} = 1$ unit, the value of which is to be determined from the total absolute flux of meteors.

The apex sources are produced by the retrograde HFC population (Jones and Brown, 1993). A value of $k_{r\mathrm{HFC}} = 14.2$ for the dust production coefficient of this population reproduces observations. Note that setting the dust production coefficient of retrograde HFCs to 14.2 times the value for JFCs does not mean that they produce 14.2 times more dust per unit time or per perihelion passage. Each comet has a dust production rate weighted by the amount of solar radiation/unit area it receives (Section 2.2.1). The model thus claims that an average retrograde HFC should produce 14.2 times more dust than the average JFC *at the same heliocentric distance*. Thus retrograde HFCs could be the same size as JFCs and 14.2 times dustier in composition, or identical in composition and have 14.2 times the area, or anywhere in between.

Since the radii of HFCs are typically a factor of 2–3 larger than those of JFCs (Lamy et al., 2004), we would expect HFCs to produce 4–9 times as much dust as JFCs simply by intercepting more sunlight and thus sublimating more material. Thus a value of $k_{r\mathrm{HFC}} = 14.2$ is consistent with retrograde HFCs having the same dust-to-gas ratio and other physical characteristics as JFCs but with somewhat larger radii (~3.8 times larger). A different dustiness is not out of the question however, as our model cannot distinguish higher dust content from larger areas subject to sublimation.

The toroidals were empirically found to be best reproduced by the six prograde Halley-family comets, together with four of the

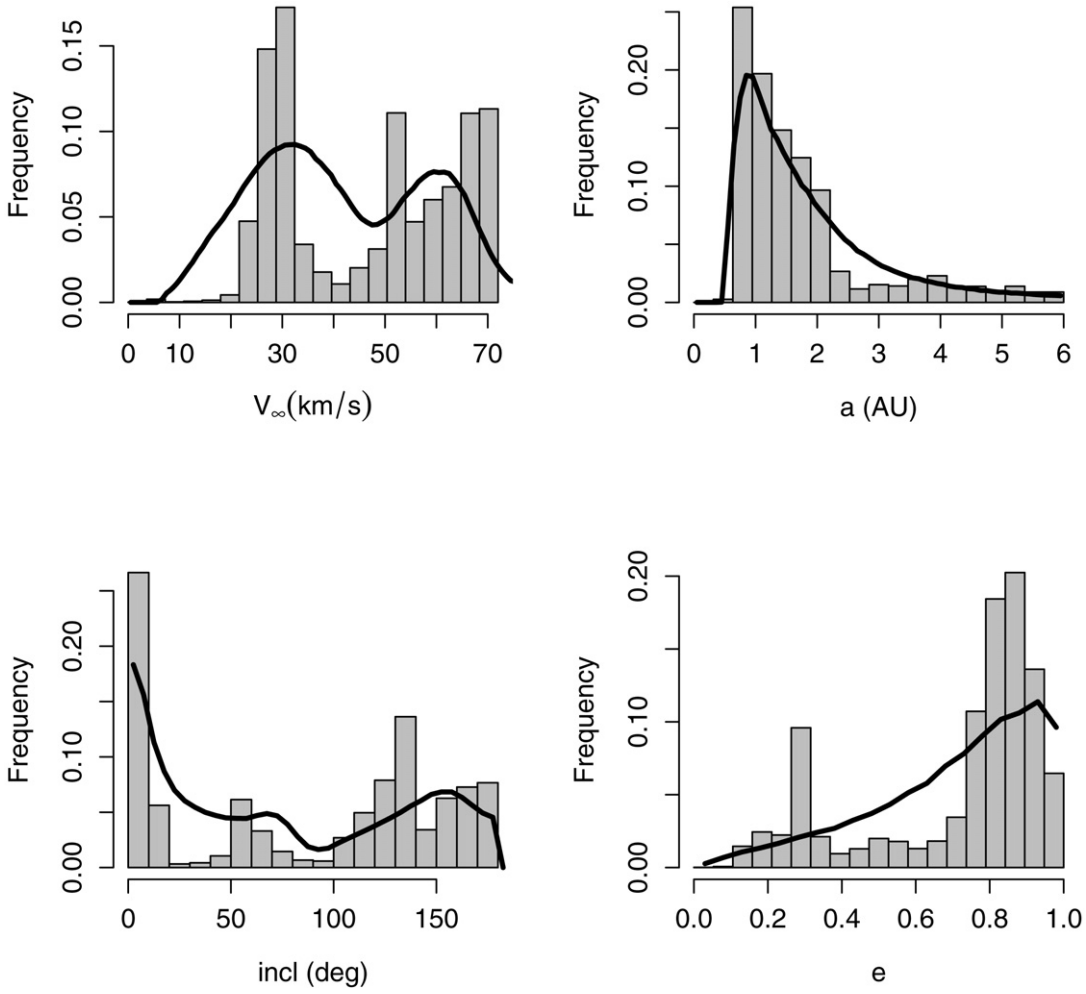

Fig. 1. The model (histogram) and CMOR observations (black line) for all meteors.

modeled NEAs, namely 2003 EH_1, 53430, 66008 and 2003 QQ_{47} (Sections 3.1.4 and 3.1.5). We take the dust production coefficient of the prograde HFCs to be the same as that determined for the retrograde HFCs ($k_{p\mathrm{HFC}} = k_{r\mathrm{HFC}} = 14.2$). With this value, the prograde HFCs produce almost exactly half the observed toroidal flux; the NEAs provide the balance. The efficiency with which the NEAs deliver meteoroids to Earth means that only very low production coefficients ($k_{\mathrm{NEA}} = 0.05$) are needed for the four NEAs to produce the other half of the toroidal flux at Earth.

This combination of parents gives an adequate representation of the toroidals, but perhaps provides the least satisfying match of the sporadic sources. The toroidals are where the potential for contributions from a defunct or undiscovered comet seems highest.

In the absence of observations of the asteroidal meteoroid population we will set the strength of the asteroidal source relative to the dust production rate of a known comet. Here we use the much-studied Comet 2P/Encke whose dust production in 1997 was determined to be $2\text{–}6 \times 10^{13}$ g per apparition or $\sim 10^{13}$ g per year (Reach et al., 2000). On the other hand, the dust released from the break-ups of the Karin and Veritas families in the asteroid belt has been calculated at 1.5×10^{18} and 3×10^{18} g respectively (Nesvorný et al., 2006), which given that they occurred 5.8 and 8.3 Myr ago translates to roughly 4×10^{11} g per year. This is believed to be supplemented by dust from other asteroid collisions to produce a total asteroidal dust production rate 3.4 times higher (Durda and Dermott, 1997), making the overall asteroid belt dust production rate approximately 10^{12} g per year. Taking the ratio of asteroidal to Encke's dust production, we set the average dust production rate of the asteroid belt to 10% that of 2P/Encke. Note that for all other parents, we chose a constant weighting factor W, but the actual dust production in the model is a function of the amount of insolation received by a particular parent. For the asteroid belt, we simply peg its dust production rate at 10% of 2P/Encke's.

4.2. Verification

The free parameters k_i are calculated to match the strengths of the observed meteor sources. However, CMOR observations provide more than simple fluxes for the sporadic complex and these provide us with a powerful tool for testing the model.

Since the free parameters k_i are chosen solely to reproduce the strengths of the sources, not their orbital elements, a comparison of the model orbital element distributions provide nearly independent tests of the model's validity.

The model and radar fluxes are presented in Figs. 1 to 4. The match is not easily quantified in a meaningful way but qualitatively, the model captures the strongest features of the sporadic complex, though there are certainly differences of detail. Much of the variation in the fine structure of the distribution can probably be attributed to the small number of parent objects of the model, only thirty-eight. Hundreds of comets (both known and long-extinct) and an unknown set of collisions within the main asteroid belt and near-Earth asteroid population have produced our Solar System's richly-structured meteoroid complex.

Please cite this article in press as: Wiegert, P., et al. A dynamical model of the sporadic meteoroid complex. Icarus (2009), doi:10.1016/j.icarus.2008.12.030

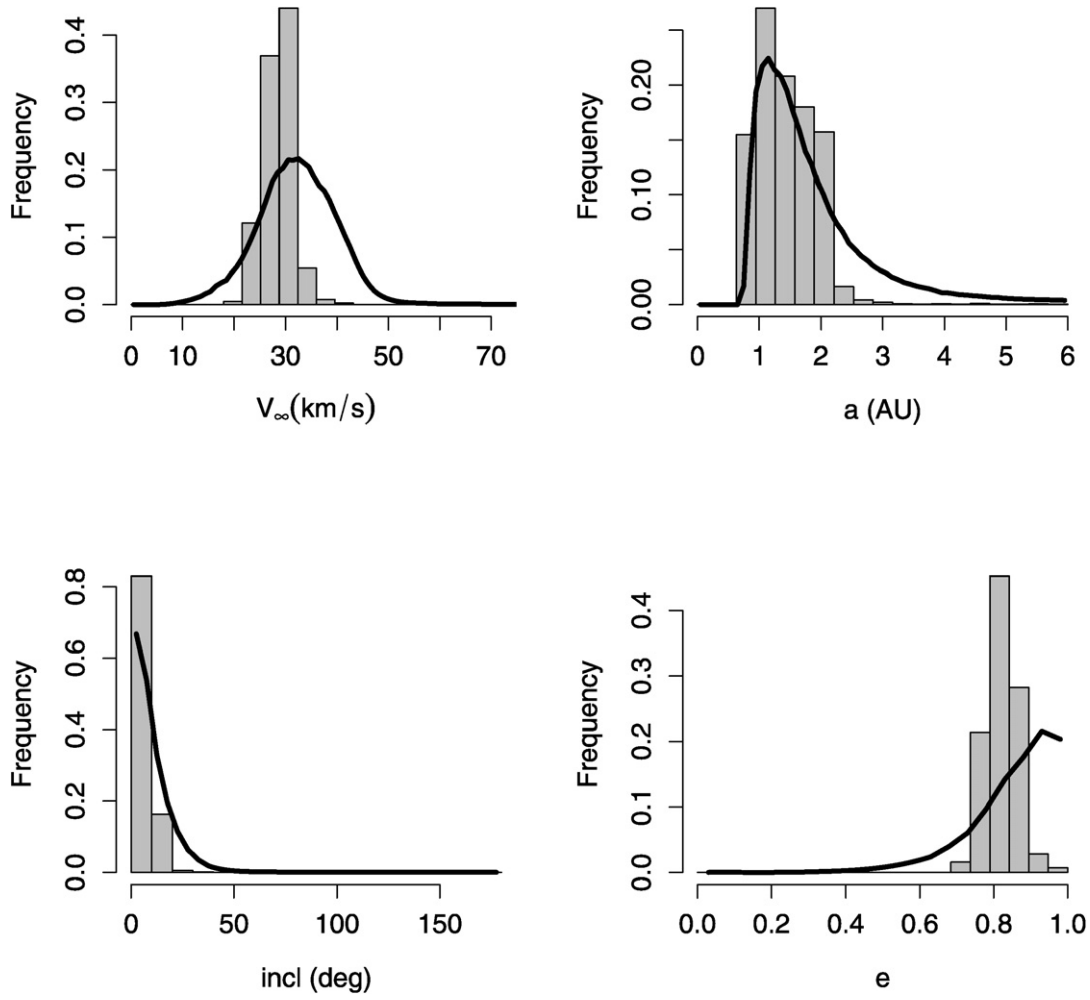

Fig. 2. The model (histogram) and CMOR observations (black line) for the helion/anti-helion meteors.

The toroidal source in particular is not easily matched by a single parent or parent population. It may be the remnants of a parent long since broken up, ejected or simply displaced to another part of the Solar System, but this will require further study.

Further testing of the model could be accomplished if other sets of observational meteor data that had been corrected for observing effects were readily available. Since the CMOR data set is among the largest and most carefully debiased data set currently available, we will take the match between it and the model (as presented in Figs. 1 to 4) to be the measure of our goodness of fit.

Despite the complexity of the origin and ongoing regeneration of the sporadic meteoroids, based on the similarity of the observations and model predictions, we conclude that our model captures the basic characteristics of the sporadic complex.

5. Discussion

5.1. The meteoroid size distribution at Earth versus that produced at the source

The model size distribution of meteoroids at the Earth is shown in Fig. 5. Though the initial size distribution of dust injected into the model is a fixed power law, the power-law nature of the distribution is not perfectly preserved over the entire size range. It has already been mentioned (Section 2.2.2) that a different size slope for ejected particles is required to match observations at the Earth. More specifically, there is an overall steepening of the distribution at Earth relative to that produced at the comet, at least at radar-observable sizes. This steeper slope indicates that smaller particles are more efficiently delivered to the Earth than larger ones. An observed differential slope of $r^{-5.0}$ ($100\ \mu m < r < 1$ cm) at Earth requires $r^{-4.6}$ distribution at the source, or equivalently, $m^{-2.34}$ at Earth requires $m^{-2.2}$ at the source. This difference is small in these terms, but nonetheless indicates that size-dependent processes play some role in the sporadic complex.

Over the full size range examined here, this difference would mean that 10 micron particles are delivered $10^{4*0.4} \approx 40$ times more efficiently than 10 cm particles. However, this slope is not maintained over the full size distribution. Fig. 5 reveals that the slope at the smallest and at the largest sizes shallows with respect to the central portion. The decreased slope at smaller sizes will be of particular interest when we examine the match between the model and observations taken by AMOR (discussed below).

In our model, the mass index for all ejected dust from all parents is set at 2.2 in order to reproduce the observed meteoroid mass index of 2.34 in the radar size range at Earth. For comparison, there are observational determinations of the mass index of dust in cometary comae. Grün et al. (2001) report $dN/dr \propto r^{-3.5-3.7}$ ($m^{-1.8-1.9}$) for dust produced by Hale–Bopp. The Giotto probe that sampled 1P/Halley's coma found the cumulative mass distribution index for large ($>10^{-9}$ kg) particles to be 0.3–0.46 ($m^{-1.30-1.46}$ or $dN/dr \propto r^{-1.9-2.38}$) though their size distribution was far from a simple power-law overall, with variations with particle size and location relative to cometary jets (McDonnell et al., 1987). Our simple choice of a mass index $s = 2.2$ for all cometary dust production implies a size distribution of fresh dust with a

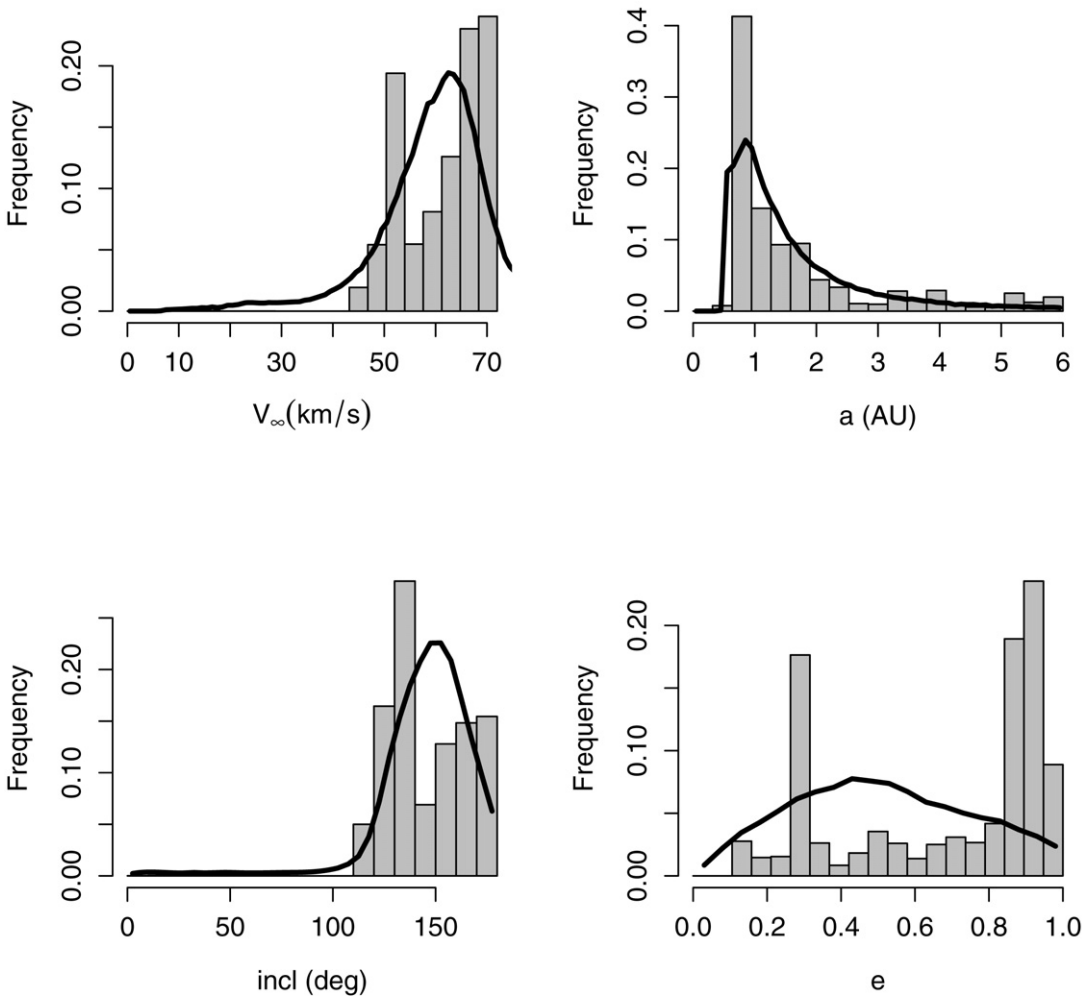

Fig. 3. The model (histogram) and CMOR observations (black line) for the apex meteors.

slope steeper than the observed values mentioned above. However, the difference is in the right direction *e.g.* the ejected distribution has a shallower slope than that of meteors at Earth. Observationally, the meteoroid mass index is steeper than that of cometary dust, and our model is qualitatively consistent with these observations.

The difference between the observed and model slopes of near-nucleus dust indicates that small particles are even more efficiently transported to Earth than our simulations indicate. This may be due to collisional fragmentation which will erode the larger sizes in favor of smaller ones, and which is expected to become quite important at sizes below 100 μm (Grun et al., 1985).

In a related vein, the Advanced Meteor Orbit Radar (AMOR) sees a shallower slope to the meteor size distribution at Earth ($s = 2.027$; Galligan and Baggaley, 2004) than the value of 2.34 quoted above, but is looking at smaller sizes ($\sim 10^{-11}$ kg or ionizations of 10^{-4} in our units). This effect is just what is expected from our model. Fig. 5 shows a change in the slope at the smallest sizes. To consider what AMOR would detect, Fig. 6 shows the size distribution of the smallest meteoroids in the model above an ionization threshold of 10^{-4} units (the result is little affected by considering all meteoroids).

A heavy line indicates the overall best fit with a lighter line indicating the fit to sizes below $r = 10^{-4}$ m. The smallest sizes in the model have a shallower slope, $dN/dr \propto -3.7$ which corresponds to a differential mass index $s = 1.9$. This is in reasonable agreement with the mass index determined by AMOR of $s = 2.027$. We conclude that at least some of the differences between the mass index measured by different techniques is due to size-dependent dynamical delivery of sporadic meteoroids.

5.2. Central condensations in the apex sources

As an example of the explanatory power of a physical model, we show how particular characteristics of the apex source first reported by the Jicamarca radial-scatter radar can be explained.

Chau et al. (2007) determined the north and south apex meteor sources contained a central condensation centered 13 degrees above/below the ecliptic, with half-widths of 3 and 9 degrees in longitude and latitude respectively (see their Fig. 1). Our model radiant distribution for the apex area is shown in Fig. 7, and shows a strong central feature in both the north and the south apex sources closely resembling those observed by Chau et al. (2007). In the absence of published values for the ionization limit of Jicamarca, we assume an ionization limit of 10^{-2} in our units, comparable to that for the ALTAIR radar (Hunt et al., 2004).

The model allows us to investigate the source of the feature by plotting the radiant distributions of the various parent objects. Fig. 8 displays the radiants due to the retrograde HFCs included in the model, and reveals that 55P/Tempel–Tuttle is the dominant source of these central enhancements. Note that these central peaks are not simply the radiants of the Leonid shower, of which 55P is the parent: the Leonid radiant is at $-2°$, $10°$ in our ecliptic coordinates. Nor are the central condensations the radiants of the Orionid, η Aquarid or Perseid showers. These showers have been

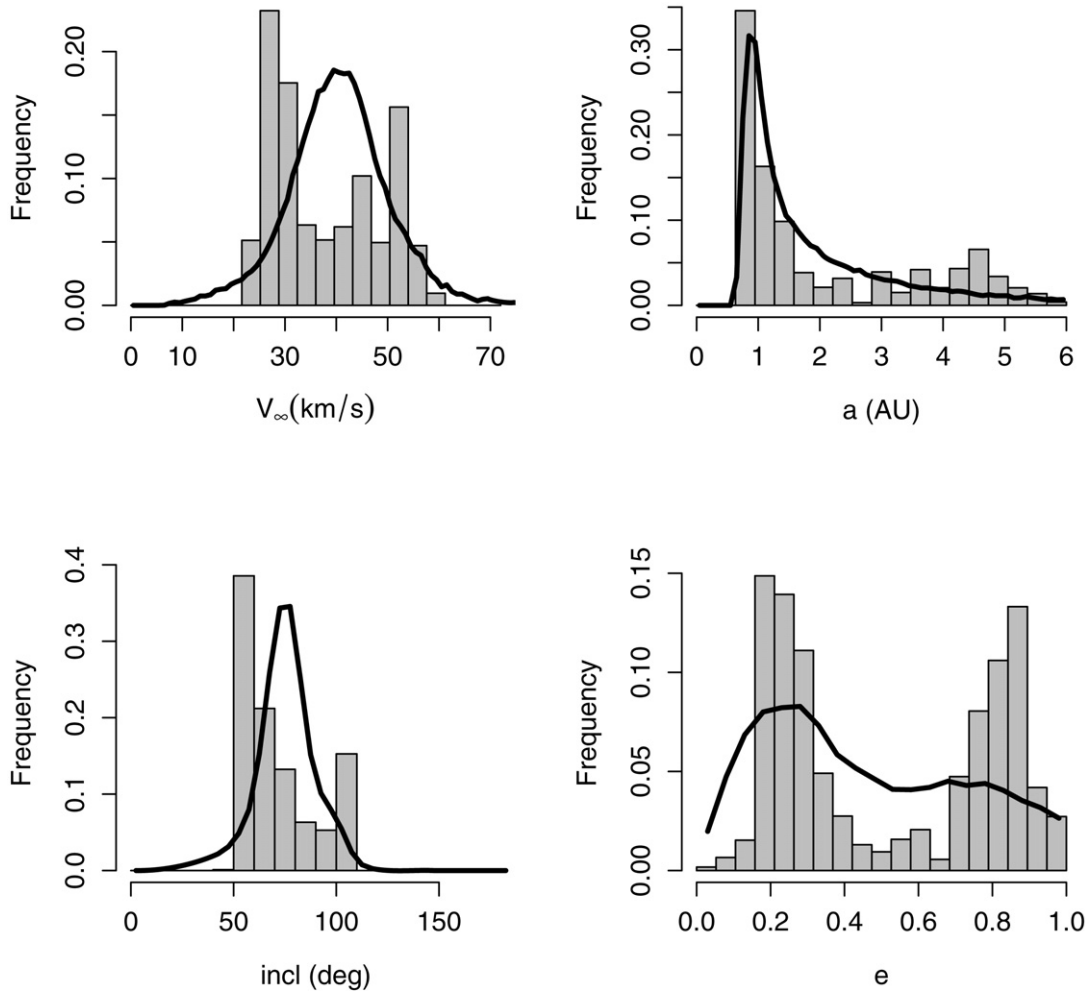

Fig. 4. The model (histogram) and CMOR observations (black line) for the toroidal meteors.

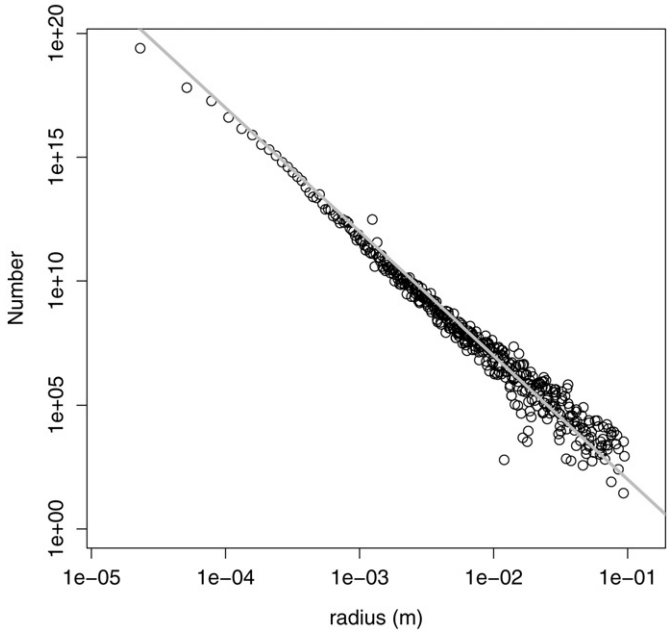

Fig. 5. The model distribution of meteoroid sizes (open circles) at the Earth. The solid line shown corresponds to $s = 2.34$. The model weight W_r is chosen to reproduce this slope between 100 μm and 1 cm (Section 2.2.2). The vertical axis is in arbitrary units.

removed as described in Section 2.2.7. A broad feature in the upper right quadrant of Fig. 7 is found to be associated with older meteoroids from 1P/Halley.

As an additional check, we can compare the eccentricity distribution of the model for these central sources with the Jicamarca results. Chau et al. (2007) found an eccentricity of 0.15–0.2. Our model results are in Fig. 9. There is a high-e component but low eccentricity orbits predominate. This is also true for meteors originating specifically from 55P, though its own eccentricity is ∼0.9. This implies the meteoroids are rather old and have evolved substantially under P–R drag. An examination of the model reveals that these central sources are indeed composed largely of small, old particles whose orbits have evolved significantly since their release. They have perihelia q near 1 AU and very high collisional probabilities with the Earth.

We conclude that the central condensations of the north and south apex sources can be adequately explained as small ($\lesssim$100 μm), old ($\gtrsim 10^5$ yr) dynamically evolved meteoroids originating from 55P/Tempel–Tuttle or an orbitally similar object.

5.3. Velocity distributions of transverse versus radial scatter radars

Radar observations of meteors can be made by at least two methods. One is transverse scatter ("meteor patrol") radar like CMOR and AMOR; the other is radial scatter ("High-Power Large Aperture" or "HPLA") radar like ALTAIR and Jicamarca. Transverse scatter radars are typically run at low power with broad beams, and the dominant detections are from specular scatter off of me-

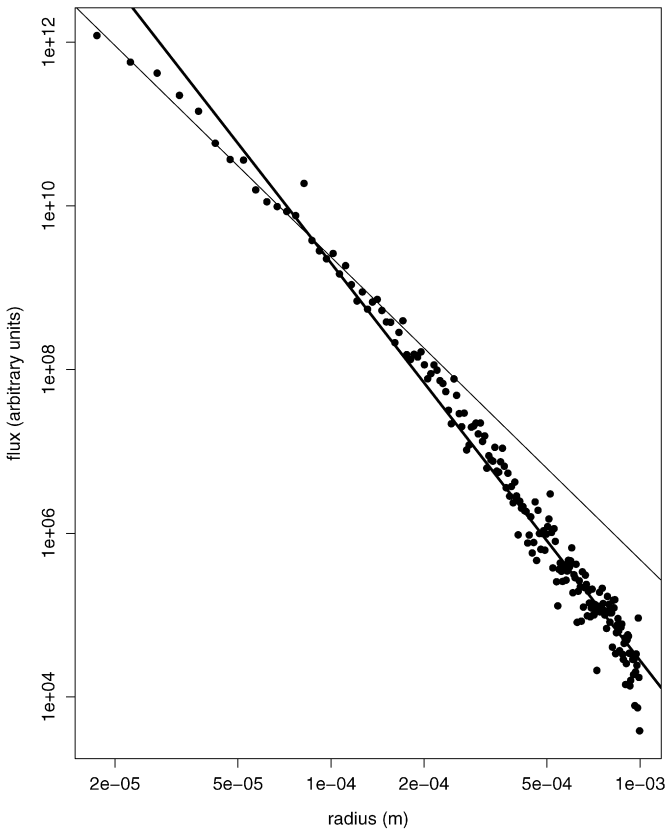

Fig. 6. The size distribution of the smallest model meteoroids above an ionization threshold of 10^{-4} units. The heavy line indicates the overall best fit slope ($dN/dr \propto r^{-5.0}$) while the thinner line indicates a least-squares fit to the region below 100 μm ($dN/dr \propto r^{-3.7}$).

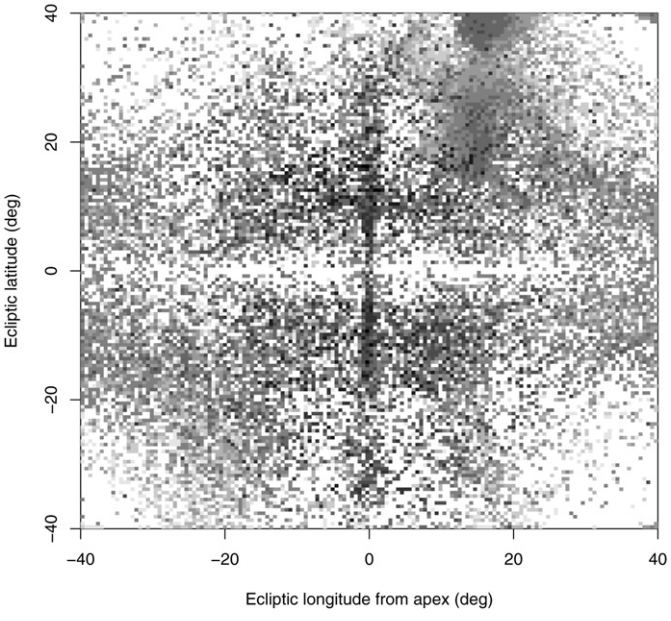

Fig. 7. Model radiant distribution near the apex for ionizations above 0.01 units.

teor trails. Because of their lower cost, they can be run for many years; the lower power also means they see larger meteoroids. Radial scatter radars use higher power and narrower beams to reflect off the ionization immediately surrounding the meteor (head echoes). The high power allows the radial scatter radars to see much smaller meteoroids, though the precise mass limits are not known for most radial scatter radars.

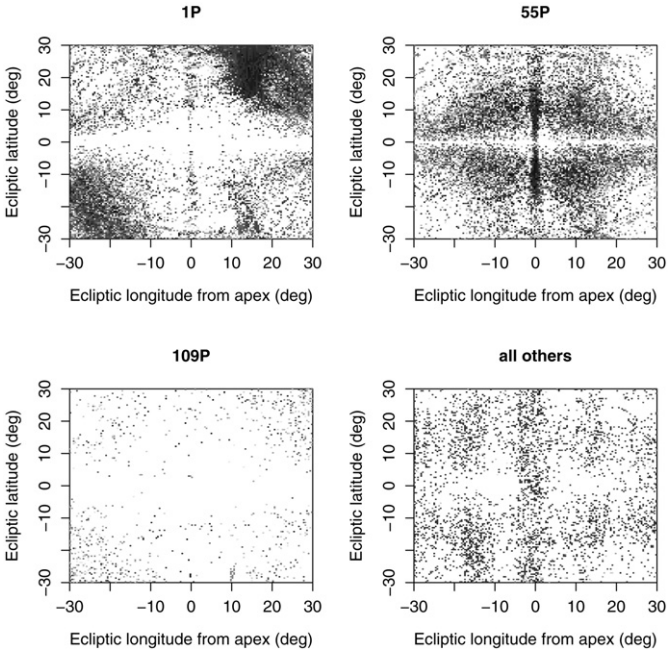

Fig. 8. Model radiant distribution near the apex broken down by parent object.

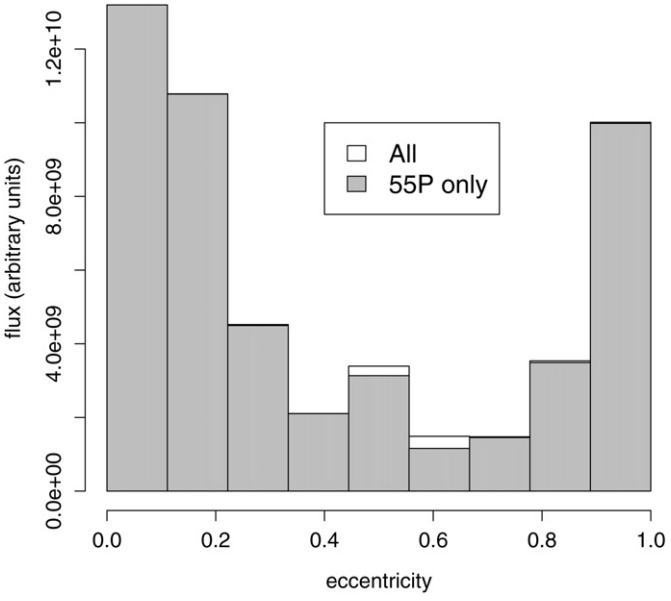

Fig. 9. Eccentricity distribution for meteors in the central condensations of the apex sources.

There have been discrepancies between the velocity distributions of meteors as measured by these two techniques that have caused some concern within the community. Though the issues involved are complex, a concise summary of the conflicting observations was made by Janches et al. (2008).

> Observations performed at various HPLA facilities around the world have resulted in faster meteor velocity distributions (Sato et al., 2000; Hunt et al., 2004; Janches et al., 2003; Chau and Woodman, 2004) than those generally derived with specular meteor radars (Taylor, 1995; Galligan and Baggaley, 2004). Specifically, HPLA velocity distributions have a bimodal shape with a prevailing peak near 55 km/s (Close et al., 2002; Janches et al., 2003; Chau et al., 2007), while most SMR velocity distri-

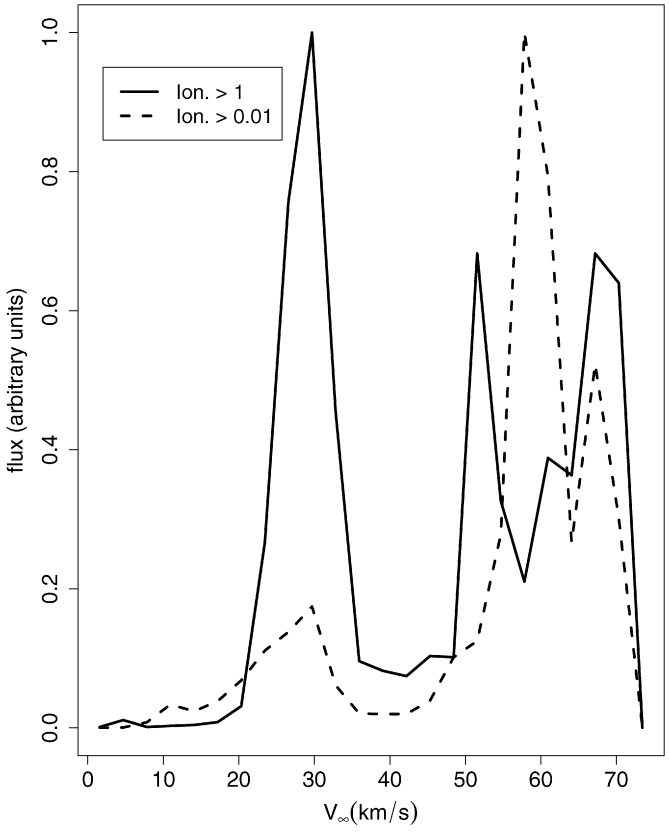

Fig. 10. The flux of meteors above certain ionization thresholds. An ionization value of unity corresponds to CMOR or the HRMP, 0.01 is the limit for ALTAIR VHF (Hunt et al., 2004; Campbell-Brown, 2008).

butions (uncorrected) have two peaks of similar magnitude at ~30 km/s and ~55 km/s (Galligan and Baggaley, 2004).

The contradictory findings could be associated with the unique observing biases associated with the different radars. In fact, it has already been shown (Hunt et al., 2004; Close et al., 2007) that a careful accounting for instrumental effects can diminish the discrepancy in the measured velocity distribution, though differences remain (Janches et al., 2008).

Here we will show that much of the difference can be attributed to the simple fact that the two techniques, because of their different sensitivities, are measuring two populations with different velocity distributions, and thus one would not expect their measurements to match.

Fig. 10 shows the model velocity distribution at an ionization threshold of 1 unit and 0.01 units. The first value is the detection cut-off for the CMOR and HRMP (Harvard Radio Meteor Project; Sekanina, Z., Southworth, R.B., 1975. Physical and dynamical studies of meteors. Meteor-fragmentation and stream-distribution studies. Technical report; Taylor, 1995; Taylor and Elford, 1998) transverse scatter radars (Campbell-Brown, 2008). The second is the limit we assume for the radial scatter radars, based on that of ALTAIR since a determination of its ionization limit as expressed here has been published (Hunt et al., 2004). The two distributions differ in just the way they are reported to in the literature. Our model predicts that radial scatter radars should see a velocity distribution with a large high velocity component, while the transverse scatter radars should see a more evenly bimodal distribution. We note here that the model distributions of Fig. 10 do not include any sophisticated analysis of the biases of a specific technique or instrument, except for different ionization cutoffs. Thus we conclude that much of the disagreement between radial and transverse radar results can be attributed to their sampling of different populations of meteoroids with inherently different velocity distributions. The underlying physical cause will be discussed in more detail in Section 5.4.

Table 2
The dominant model components of each of the traditional sporadic sources at two ionization cutoffs. The fraction column shows the percentage of each source which is contributed by the dominant parent.

Source	Ion. > 1		Ion. > 0.01	
	Parent	Fraction	Parent	Fraction
Total	2P	30%	55P	78%
Anti-helion	2P	94%	2P	80%
Helion	2P	95%	2P	82%
N. apex	55P	50%	55P	96%
S. apex	109P	39%	55P	95%
N. toroidal	66008	35%	2003 QQ_{47}	58%
S. toroidal	12P	25%	8P	25%
Other	8P	21%	55P	23%

5.4. Strongest contributors to the sporadic sources

One question our model can answer is: which are the dominant contributors to the sporadic meteoroid complex at the Earth? This depends quite strongly on one's observational technique. Table 2 shows the dominant contributors in terms of number of meteors per unit time down to ionization limits of 1 and 0.01 units. At the higher threshold more relevant to transverse scatter radar and visual detection we see that 2P/Encke is the overall leader producing fully 30% of all meteors. The lower threshold produces a completely different result, as now 55P/Tempel–Tuttle dominates with a strong majority of 78% of the total meteor flux by number. This is of course at the heart of the different velocity distributions seen by transverse and radial scatter radars (Section 5.3).[1]

Transverse scatter radars see a sporadic meteor sky where 2P/Encke is the largest contributor, producing 30% of all meteors, thus the helion/anti-helion sources are prominent. Radial scatter radars see a sky dominated by 55P/Tempel–Tuttle, which produces about 4 of every 5 meteors above their ionization threshold. Thus radial scatter radars should measure a velocity distribution heavy in high-velocity meteors. As well, weak (but not absent) anti-helion/helion sources and a dominant apex source with central condensations within it are precisely what our model would predict radial scatter radars would observe, and all are consistent with observations (Chau et al., 2007).

It is probably worth noting here that the dominance of these two comets in producing the sporadic complex sheds much doubt on the standard hypothesis (one we made ourselves in the construction of this model) that the sporadics are supplied by the general cometary population as a whole. It seems that they are rather the products of a small number of comets with high-transfer efficiencies to near-Earth space.

5.5. The ring

One feature of the sporadic meteors recently observed by CMOR is the presence of a ring centered on the Earth's apex with a radius of approximately 55° (Campbell-Brown, 2008). The ring is much weaker than the traditional sporadic sources and varies in strength throughout the year.

[1] We remind the reader again that 2P/Encke represents itself as well as three other comets in the model. As a result, our model can only attribute this flux to 2P/Encke and its bin members (73P/Schwassmann–Wachmann, 141P/Machholz and 169P/NEAT) representing the lowest perihelion and smallest semimajor axis JFCs. (See Table 1.)

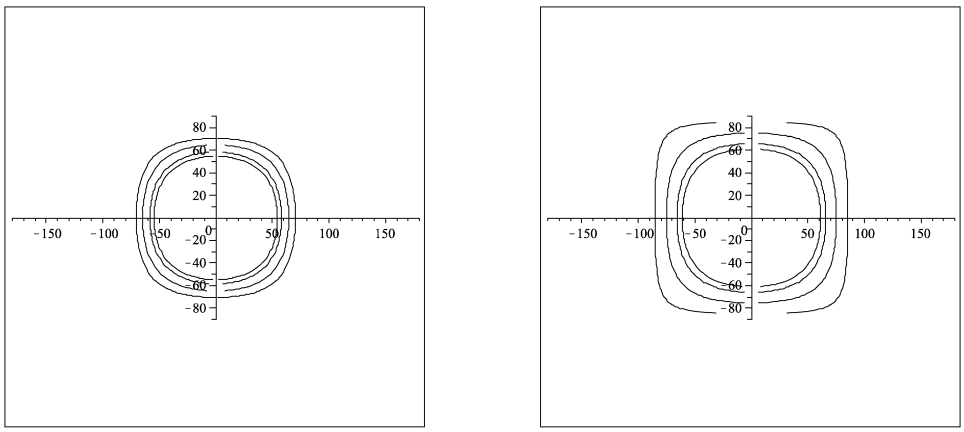

Fig. 11. The allowed radiants of meteoroids with $h \in \{0.11, 0.2, 0.4, 0.6\}$ for (a) $a = 1$ AU and (b) $a = 1.5$ AU, centered on the Earth's apex direction. Axes are labeled in degrees.

We were able to determine that the ring is a dynamical phenomenon resulting from the Kozai effect (Kozai, 1962; Kinoshita and Nakai, 1999) also known as the secular precession effect discussed by Babadzhanov and Obrubov (1987). This effect produces out-of-phase oscillations of e and i and will approximately conserve both a and the quantity

$$h = \sqrt{1 - e^2} \cos i. \tag{8}$$

One can compute the possible radiants for high-inclination dust under the Kozai constraint of Eq. (8). Plots of the geometrically allowed radiant directions for a variety of h values are presented in Fig. 11 for dust semimajor axes of 1 and 1.5 AU.

As the dust spirals in towards the Sun under P–R drag, it reaches its maximum impact probability with the Earth near $a =$ 1 AU and so we expect the strongest ring feature will be associated with this dust. In fact, CMOR shows the radiants in the ring have an average semimajor axis of 1 AU (Campbell-Brown, 2008). And as can be seen by Fig. 11a, such dust is expected to produce radiants clustered heavily between 50 and 60°, as observed. Thus we conclude that the ring is a collective effect of high-inclination dust (possibly from a variety of parents), evolving under P–R drag and the Kozai effect.

5.6. Strength asymmetry between the anti-helion and helion sources

A long-standing question has been the origin of the strength asymmetry of the helion and anti-helion sources (Keay, 1963; Stohl et al., 1968; Jones and Brown, 1993). The ratio of the fluxes from the anti-helion and helion sources as seen by CMOR is 1.3. Other surveys (not all corrected) have ratios reported from 1.2 to 2.3 (see Jones and Brown, 1993, and references therein). This effect has sometimes been ascribed to day/night variations in radar sensitivity, but our model indicates that the asymmetry may be intrinsic. A plot of the anti-helion/helion flux ratio from our model at different masses is shown in Fig. 12.

The model predicts a relatively small asymmetry at larger masses, which increases at sizes smaller than 10^{-6} kg. Thus we would expect that any technique which can see significantly beyond this mass limit should see an increasing asymmetry between the two sources. Since smaller particles are more abundant, we would expect that the ratio observed would be close to the model ratio for the smallest masses detectable with the technique in question. For the CMOR radar, this is in the 10^{-7} to 10^{-8} kg range, giving an expected AH/HE ratio of 1.2, in line with observations. Thus the AH/HE asymmetry can be accounted for on dynamical grounds without appealing to arguments of time-varying radar sensitivity.

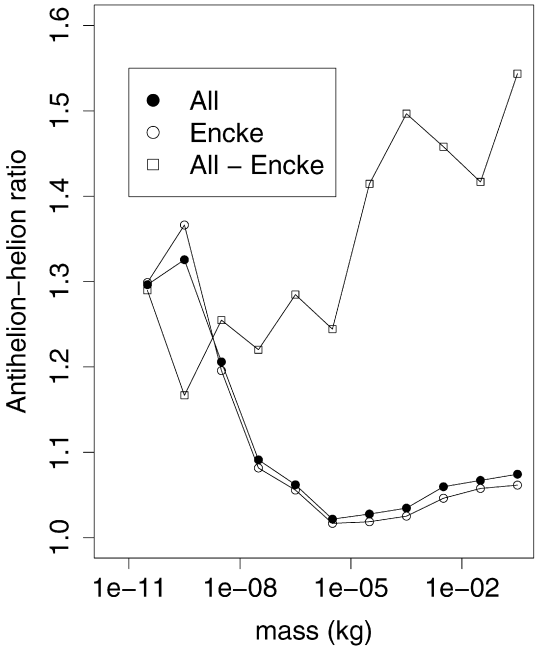

Fig. 12. The ratio of the model flux of the anti-helion source relative to the helion source at different meteoroid masses (filled circles). The open circles are the values for 2P/Encke (which is the dominant contributor to the helion/anti-helion sources), the open squares represent the set from which Encke's meteoroids are excluded.

Since the anti-helion and helion meteors originate from the same source, the existence of such an asymmetry is somewhat puzzling. We consider the possibility that our algorithm for extracting meteors from the simulations is biased since a single meteoroid orbit may be linked to two possible radiants, one within the helion and the other within the anti-helion sources. Our algorithm is specifically constructed to allow any meteor to correctly register either zero, one or two passages within 0.1 AU of the Earth, in order to allow meteors which might contribute to both the helion and anti-helion sources to be counted correctly. In computing the ratio of inward to outward moving meteoroids at the Earth for other samples, we find it is near unity (1 ± 0.05) in all other cases. Thus, we conclude that the anti-helion/helion asymmetry is a real dynamical effect and not associated with our method of selecting meteoroids from the simulated sample.

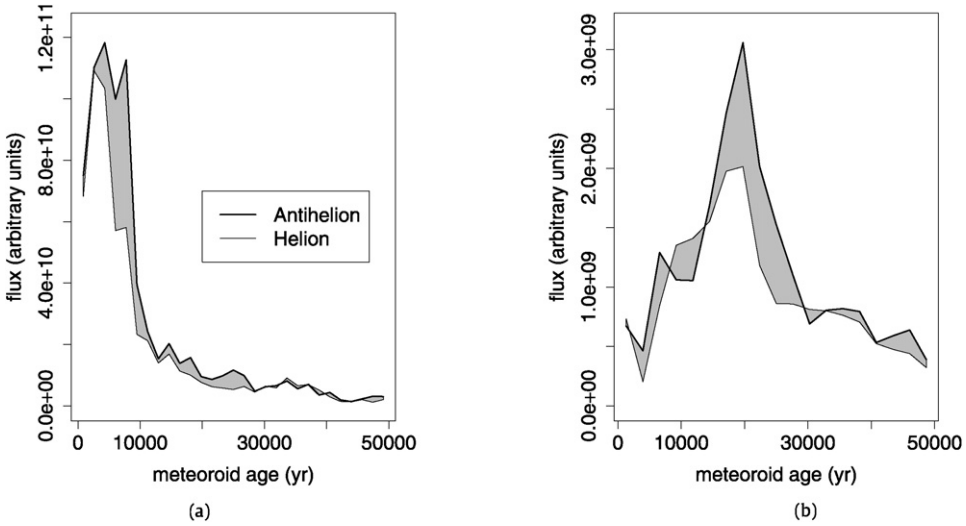

Fig. 13. The fluxes of the anti-helion and helion sources for meteoroids of different ages, (a) all sizes (left panel), (b) radii $>$ 50 μm (right panel). The heavy line is the anti-helion flux, the thinner line, the helion flux. Gray is used to shade the area between the two curves.

Since 2P/Encke is the dominant contributor to the anti-helion/helion source, the asymmetry can be traced back to it. As seen in Fig. 12, 2P also shows a shift to a high anti-helion/helion ratio at small masses. The anti-helion/helion asymmetry may thus simply be the result of size-dependent delivery processes from Comet 2P/Encke, since 2P contributes >90% of all helion and anti-helion meteoroids in our model at CMOR's limiting ionization (see Section 5.4 for more details).

The asymmetry can be linked to relatively young meteoroids ($\lesssim$10 thousand yr old) as shown in Fig. 13. The asymmetry peaks at meteoroid ages of several thousand years, comparable to the precession period of Encke itself (∼5000 yr) and seems to preclude short-term effects associated with the particular initial conditions chosen for Encke's orbit. The association with smaller sizes points to a β-related effect. This is supported by the fact that at larger sizes, the asymmetry weakens and is associated with older particles. Fig. 13b shows the fluxes for particles larger than 50 μm. In this case, the difference between the sources is less pronounced and associated with meteoroids near 20000 yr in age. At larger sizes, the asymmetry continues to diminish and is essentially gone at sizes with $r > 250$ μm.

In a more general context, we note that the anti-helion/helion sources themselves are easily seen in the radiant plots of any of the JFCs modeled. They are a collective behavior common to all JFCs. The *asymmetry* is a different story. Since a single comet (2P/Encke) is such a large contributor to the model asymmetry, there is a danger that some other unmodeled JFCs also has a role to play that we have missed here. In particular, we note that in Fig. 12 the anti-helion/helion ratio of all other sources excluding 2P is also substantially larger than unity. Thus a past outburst from a different JFC could also account for the asymmetry. In this case better information about cometary dust production rates and their time variability may be necessary to disentangle this issue.

However, given that 2P/Encke is such a strong contributor to the anti-helion/helion sources (see Section 5.4 for more), we consider it likely that it (or a lost comet on a similar orbit) is the primary cause. We conclude that the anti-helion/helion strength asymmetry observed at Earth is probably associated with the P–R drag evolution of meteoroids released from 2P/Encke or an orbitally similar object over the last 4000–20000 years. A full answer to this question is beyond the scope of this paper but certainly deserves further study.

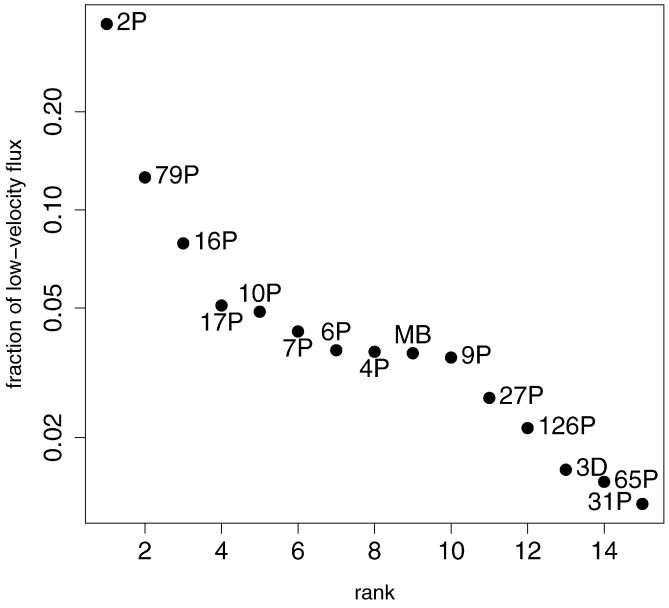

Fig. 14. A ranked plot of the primary contributors to the low velocity flux ($V_\infty <$ 15 km/s) at Earth. MB represents the main asteroid belt.

5.7. The low-velocity flux at Earth

In Section 4.1, the difficulty in using the observed meteor flux at Earth in order to determine the dust production rate in the main asteroid belt was discussed. We resorted rather to a weighting of the asteroid belt's dust production based on a direct comparison of the dust production rate associated with recent asteroid family break-ups with that of 2P/Encke. Coupled with the inherent stochasticity of asteroidal dust production (assuming it is collisionally produced) the asteroidal k_{MBA} is the least well-constrained of our dust production coefficients. However, based on our best guess of the asteroidal dust production, we can ask the question "How much of the meteoroid flux at Earth is asteroidal?"

Of the total flux, asteroidal dust comprises 1.3% by number (all sizes). This is mostly confined to low velocities. Fig. 14 shows the largest contributors to the flux of meteors with $V_\infty < 15$ km/s. Surprisingly, 2P/Encke is the largest contributor with approximately 50% of the total, followed by 79P/duToit–Hartley. The as-

teroidal contribution in our model hovers around 4%, which is consistent with the results from the ESA model (Dikarev et al., 2004).

The fraction of asteroidal dust in our model obviously depends strongly on the dust production we have assumed, here taken to be only 10% of the dust production of 2P/Encke. If the asteroid belt produces, say, one Encke-equivalent of dust per year on average, then the asteroid belt becomes equivalent to 2P/Encke in terms of contribution to the low velocity flux near Earth.

In particular we note that there is chemical and physical evidence that substantial numbers of IDPs are asteroidal in nature (Zolensky and Barrett, 1994). Modeling of the IRAS dust bands indicates that 30% of the zodiacal cloud may be dust spiralling in from the main belt (Dermott et al., 2002b). For our chosen parameters, asteroids contribute only 4% of the spatial number density of meteoroids near the Earth, but this result is sensitive to the poorly-known dust production rate of the asteroid belt.

6. Conclusions

A physics-based model has been developed that follows the paths of meteoroids produced within the Solar System from their initial release through their final demise. The model includes radiation effects, collisions and gravitational perturbations due to all the major planets. The free parameters of the model are the size index of cometary dust as well as the production coefficients of the different parent populations. These model parameters are calibrated to observations of the sporadic sources from the CMOR transverse scatter radar.

The resulting parent dust production rates are reasonable, with the HFCs expected to produce an order of magnitude more dust under similar insolation conditions, consistent with their typically larger size. The toroidal sources prove to be most problematic but can be modeled rather well by the prograde HFCs together with additional dust production from some high-inclination near-Earth objects, though their origin with a now-defunct high-inclination comet remains a distinct possibility. The model size index that is derived is consistent with observations of a shallower size index at the cometary nucleus versus that observed at Earth and indicates that small particles are delivered more efficiently to Earth than larger ones. At the same time, a shift in the model slope at the very smallest sizes ($\sim 10^{-11}$ kg or ionizations of 10^{-4} units) may explain why observations by AMOR show a much flatter index than those with higher thresholds.

The model also points to a resolution of the ongoing conflict between observations taken by transverse and radial scattering radars. Although each measures different velocity distributions, this can be attributed to their different ionization thresholds. Radial scatter radars should see a sky strongly dominated by small fast apex meteors from 55P/Tempel–Tuttle. Transverse scattering radars should see primarily larger helion/anti-helion meteors originating from 2P/Encke, though a strong component from other parents is also expected to be present. Thus the two techniques are complementary in that they measure different components of the sporadic meteor population.

The ring seen centered on the apex with a radius of 55° is caused by high-inclination meteoroids undergoing Kozai oscillation. The source of the helion/anti-helion asymmetry observed at meteor patrol radar sizes can be largely explained as a result of different dynamical delivery efficiencies of relatively young meteoroids from 2P/Encke.

Though this model has provided some insight into the sporadic meteor flux at Earth, there remain more questions to be addressed. Clearly, the evolution of meteoroid streams from the parents modeled here can be examined individually. But there is more to do concerning the sporadic complex as well. For example, our results to date have not considered the fact that the sporadic flux is not axisymmetric around the Sun: it is known to vary throughout the year by about ±30% (Campbell-Brown and Jones, 2006). This time variability may be attributed to unequal contributions from different parents and it is a feature we plan to investigate.

Beyond the meteoroid population at Earth, this model will also allow us to investigate the expected sporadic flux at other planets (*e.g.* Mars). The distribution of dust throughout the Solar System, among the inner planets as well as the outer, is also inherent in the model and can be used refine the collisional lifetimes of meteoroids. Moving beyond meteor physics, the model can address questions related to the intensity of zodiacal light and the contamination of infrared and longer-wavelength images taken as part of galactic, extra-galactic or cosmological studies.

Acknowledgments

We thank David Asher and an anonymous referee for their thorough reviews which much improved this work. This research was supported in part by the NASA Meteoroid Environment Office and the Natural Sciences and Engineering Research Council of Canada.

References

Babadzhanov, P.B., Obrubov, I.V., 1987. Evolution of meteoroid streams. In: Ceplecha, Z., Pecina, P. (Eds.), European Regional Astronomy Meeting of the IAU, vol. 2. Czechoslovak Academy of Sciences, Springer-Verlag, Ondrejov, Czechoslovakia, pp. 141–150.

Campbell-Brown, M.D., 2008. High resolution radiant distribution and orbits of sporadic radar meteoroids. Icarus 196, 144–163.

Campbell-Brown, M.D., Jones, J., 2006. Annual variation of sporadic radar meteor rates. Mon. Not. R. Astron. Soc. 367, 709–716.

Chambers, J.E., 1999. A hybrid symplectic integrator that permits close encounters between massive bodies. Mon. Not. R. Astron. Soc. 304, 793–799.

Chau, J.L., Woodman, R.F., 2004. Observations of meteor head-echoes using the Jicamarca 50 MHz radar in interferometer mode. Atmos. Chem. Phys. 4, 511–521.

Chau, J.L., Woodman, R.F., Galindo, F., 2007. Sporadic meteor sources as observed by the Jicamarca high-power large-aperture VHF radar. Icarus 188, 162–174.

Close, S., Oppenheim, M., Hunt, S., Dyrud, L., 2002. Scattering characteristics of high-resolution meteor head echoes detected at multiple frequencies. J. Geophys. Res. (Space Phys.) 107, 1295–1306.

Close, S., Brown, P., Campbell-Brown, M., Oppenheim, M., Colestock, P., 2007. Meteor head echo radar data: Mass velocity selection effects. Icarus 186, 547–556.

Crifo, J.F., Rodionov, A.V., 1997. The dependence of the circumnuclear coma structure on the properties of the nucleus. Icarus 127, 319–353.

Delsemme, A.H., 1982. Chemical composition of cometary nuclei. In: Wilkening, L.L. (Ed.), Comets. University of Arizona Press, Tucson, pp. 85–130.

Dermott, S.F., Durda, D.D., Grogan, K., Kehoe, T.J.J., 2002a. Asteroidal dust. In: Asteroids III. University of Arizona Press, Tucson, pp. 423–442.

Dermott, S.F., Kehoe, T.J.J., Durda, D.D., Grogan, K. Nesvorný, D., 2002b. Recent rubble-pile origin of asteroidal Solar System dust bands and asteroidal interplanetary dust particles. In: Warmbein, B. (Ed.), Asteroids, Comets, and Meteors: ACM 2002. ESA Special Publication, vol. 500, pp. 319–322.

Dikarev, V., Jehn, R., Grün, E., 2002. Towards a new model of the interplanetary meteoroid environment. Adv. Space Res. 29, 1171–1175.

Dikarev, V., Grün, E., Baggaley, J., Galligan, D., Landgraf, M., Jehn, R., 2004. Modeling the sporadic meteoroid background cloud. Earth Moon Planets 95, 109–122.

Durda, D.D., Dermott, S.F., 1997. The collisional evolution of the asteroid belt and its contribution to the zodiacal cloud. Icarus 130, 140–164.

Everhart, E., 1985. An efficient integrator that uses Gauss–Radau spacings. In: Carusi, A., Valsecchi, G.B. (Eds.), Dynamics of Comets: Their Origin and Evolution. Kluwer, Dordrecht, pp. 185–202.

Galligan, D.P., Baggaley, W.J., 2004. The orbital distribution of radar-detected meteoroids of the Solar System dust cloud. Mon. Not. R. Astron. Soc. 353, 422–446.

Grun, E., Zook, H.A., Fechtig, H., Giese, R.H., 1985. Collisional balance of the meteoritic complex. Icarus 62, 244–272.

Grün, E., Hanner, M.S., Peschke, S.B., Müller, T., Boehnhardt, H., Brooke, T.Y., Campins, H., Crovisier, J., Delahodde, C., Heinrichsen, I., Keller, H.U., Knacke, R.F., Krüger, H., Lamy, P., Leinert, C., Lemke, D., Lisse, C.M., Müller, M., Osip, D.J., Solc, M., Stickel, M., Sykes, M., Vanysek, V., Zarnecki, J., 2001. Broadband infrared photometry of Comet Hale–Bopp with ISOPHOT. Astron. Astrophys. 377, 1098–1118.

Hunt, S.M., Oppenheim, M., Close, S., Brown, P.G., McKeen, F., Minardi, M., 2004. Determination of the meteoroid velocity distribution at the Earth using high-gain radar. Icarus 168, 34–42.

Janches, D., Nolan, M.C., Meisel, D.D., Mathews, J.D., Zhou, Q.H., Moser, D.E., 2003. On the geocentric micrometeor velocity distribution. J. Geophys. Res. (Space Phys.) 108, 1222–1235.

Janches, D., Close, S., Fentzke, J.T., 2008. A comparison of detection sensitivity between ALTAIR and Arecibo meteor observations: Can high power and large aperture radars detect low velocity meteor head-echoes. Icarus 193, 105–111.

Jenniskens, P., 2004. 2003 EH1 is the Quadrantid shower parent comet. Astron. J. 127, 3018–3022.

Jones, J., Brown, P., 1993. Sporadic meteor radiant distributions—Orbital survey results. Mon. Not. R. Astron. Soc. 265, 524–532.

Jones, J., Brown, P., Ellis, K.J., Webster, A.R., Campbell-Brown, M., Krzemenski, Z., Weryk, R.J., 2005. The Canadian Meteor Orbit Radar: System overview and preliminary results. Planet. Space Sci. 53, 413–421.

Keay, C.S.L., 1963. The distribution of meteors around the Earth's orbit. Mon. Not. R. Astron. Soc. 126, 165–176.

Kinoshita, H., Nakai, H., 1999. Analytical solution of the Kozai resonance and its application. Celest. Mech. Dynam. Astron. 75, 125–147.

Kozai, Y., 1962. Secular perturbations of asteroids with high inclination and eccentricity. Astron. J. 67, 591–598.

Lamy, P.L., Toth, I., Fernandez, Y.R., Weaver, H.A., 2004. The sizes, shapes, albedos, and colors of cometary nuclei. In: Comets II. University of Arizona Press, Tucson, pp. 223–264.

Landgraf, M., Jehn, R., Altobelli, N., Dikarev, V., Grün, E., 2001. Interstellar dust module for the ESA meteoroid model. In: Sawaya-Lacoste, H. (Ed.), Space Debris. ESA Special Publication, vol. 473, pp. 227–229.

Marsden, B.G., Williams, G.V., 2005. Catalogue of Cometary Orbits, 16th ed. IAU Central Bureau for Astronomical Telegrams—Minor Planet Center, Cambridge, MA.

McDonnell, J.A.M., Evans, G.C., Evans, S.T., Alexander, W.M., Burton, W.M., Firth, J.G., Bussoletti, E., Grard, R.J.L., Hanner, M.S., Sekanina, Z., 1987. The dust distribution within the inner coma of Comet P/Halley 1982i—Encounter by Giotto's impact detectors. Astron. Astrophys. 187, 719–741.

Nesvorný, D., Vokrouhlický, D., Bottke, W.F., Sykes, M., 2006. Physical properties of asteroid dust bands and their sources. Icarus 181, 107–144.

Öpik, E.J., 1976. Interplanetary Encounters—Close-Range Gravitational Interactions. Developments in Solar System and Space Science. Elsevier, Amsterdam.

Reach, W.T., Sykes, M.V., Lien, D., Davies, J.K., 2000. The formation of Encke meteoroids and dust trail. Icarus 148, 80–94.

Sato, T., Nakamura, T., Nishimura, K., 2000. Orbit determination of meteors using the MU radar. IEICE Trans. Commun. E83-B (9), 1990–1995.

Spinrad, H., 1987. Comets and their composition. Annu. Rev. Astron. Astrophys. 25, 231–269.

Steel, D.I., Elford, W.G., 1986. Collisions in the Solar System. III. Meteoroid survival times. Mon. Not. R. Astron. Soc. 218, 185–199.

Stohl, J., 1968. Seasonal variation in the radiant distribution of meteors. In: Kresak, L., Millman, P.M. (Eds.), Physics and Dynamics of Meteors. IAU Symposium, vol. 33, pp. 298–303.

Taylor, A.D., 1995. The Harvard Radio Meteor Project velocity distribution reappraised. Icarus 116, 154–158.

Taylor, A.D., Elford, W.G., 1998. Meteoroid orbital element distributions at 1 AU deduced from the Harvard Radio Meteor Project observations. Earth Planets Space 50, 569–575.

Vaubaillon, J., Lamy, P., Jorda, L., 2006. On the mechanisms leading to orphan meteoroid streams. Mon. Not. R. Astron. Soc. 370, 1841–1848.

Vedder, J.D., 1998. Main belt asteroid collision probabilities and impact velocities. Icarus 131, 283–290.

Whipple, F.L., 1967. On maintaining the meteoritic complex. In: Zodiacal Light and the Interplanetary Medium. NASA-SP150, pp. 409–426.

Wiegert, P., Brown, P., 2005. The Quadrantid meteoroid complex. Icarus 179, 139–157.

Williams, I.P., Ryabova, G.O., Baturin, A.P., Chernitsov, A.M., 2004. The parent of the Quadrantid meteoroid stream and Asteroid 2003 EH1. Mon. Not. R. Astron. Soc. 355, 1171–1181.

Wisdom, J., Holman, M., 1991. Symplectic maps for the n-body problem. Astron. J. 102, 1528–1538.

Zolensky, M.E., Barrett, R.A., 1994. Compositional variations of olivines and pyroxenes in chondritic interplanetary dust particles. Meteoritics 29, 616–620.

Please cite this article in press as: Wiegert, P., et al. A dynamical model of the sporadic meteoroid complex. Icarus (2009), doi:10.1016/j.icarus.2008.12.030